SECONIC: Towards multi-compartmental models for ultrasonic brain stimulation by intramembrane cavitation

Thomas Tarnaud, Wout Joseph, Ruben Schoeters, Luc Martens, Emmeric Tanghe

***Abstract*—*Objective*: To design a computationally efficient model for ultrasonic neuromodulation (UNMOD) of morphologically realistic multi-compartmental neurons based on intramembrane cavitation. *Approach*: A Spatially Extended Neuronal Intramembrane Cavitation model that accurately predicts observed fast Charge Oscillations (SECONIC) is designed. A regular spiking cortical Hodgkin-Huxley type nanoscale neuron model of the bilayer sonophore and surrounding proteins is used. The accuracy and computational efficiency of SECONIC is compared with the Neuronal Intramembrane Cavitation Excitation (NICE) and multiScale Optimized model of Neuronal Intramembrane Cavitation (SONIC). *Main results*: Membrane charge redistribution between different compartments should be taken into account via fourier series analysis in an accurate multi-compartmental UNMOD-model. Approximating charge and voltage traces with the harmonic term and first two overtones results in reasonable goodness-of-fit, except for high ultrasonic pressure (adjusted R-squared ≥ 0.61). Taking into account the first eight overtones results in a very good fourier series fit (adjusted R-squared ≥ 0.96) up to 600 kPa. Next, the dependency of effective voltage and rate parameters on charge oscillations is investigated. The two-tone SECONIC-model is one to two orders of magnitude faster than the NICE-model and demonstrates accurate results for ultrasonic pressure up to 100 kPa. *Significance*: Up to now, the underlying mechanism of UNMOD is not well understood. Here, the extension of the bilayer sonophore model to spatially extended neurons via the design of a multi-compartmental UNMOD-model, will result in more detailed predictions that can be used to validate or falsify this tentative mechanism. Furthermore, a multi-compartmental model for UNMOD is required for neural engineering studies that couple finite difference time domain simulations with neuronal models. Here, we propose the SECONIC-model, extending the SONIC-model by taking into account charge redistribution between compartments.**

***Index Terms*—Ultrasonic neuromodulation (UNMOD), bilayer sonophore, intramembrane cavitation, computational modeling, nanoscale multi-compartmental models, multiscale optimization**

This work was carried out using the Supercomputer Infrastructure (STEVIN) at Ghent University, funded by Ghent University, the Flemish Supercomputer Center (VSC), the Hercules Foundation and the Flemish Government department EWI.

This research was funded by the FWO-project G046816N. T. Tarnaud is a PhD Fellow of the FWO-V (SB) (Research Foundation Flanders, Belgium). R. Schoeters is a PhD Fellow of the FWO-V (Research Foundation Flanders, Belgium).

T. Tarnaud, W. Joseph, R. Schoeters, L. Martens, and E. Tanghe are with the Department of Information Technology (INTEC-WAVES/IMEC), Ghent University/IMEC, Technologypark 126, 9052 Zwijnaarde, Belgium. E-mail: thomas.tarnaud@ugent.be

I. Introduction

ULTRASONIC neuromodulation or UNMOD is a promising alternative to conventional electrical brain stimulation, due to its high spatial resolution, non-invasiveness, good safety profile and smaller inter-subject variability of pressure fields [1]–[17]. Also, the idea to use ultrasonic neuromodulation as a non-invasive alternative of conventional deep brain stimulation (deep UNMOD) has been proposed [6], [7], [18]–[22], based on the fact that multiple-element phased tranducers are succesfully used for subthalamotomy or tumour ablation with millimeter precision [23]–[26]. However, neural engineering studies for UNMOD have been hindered by a lack of understanding of the underlying mechanism. Although several tentative mechanisms have been proposed, the interactions between them is not yet clear [27]–[37]. Furthermore, it would be helpful to understand under which conditions (ultrasonic waveform, neuron types…) a tentative mechanism is more dominant. Here, computational simulations help to separate the effects of different proposed actions by which acoustical waves modulate neuronal activity. In this study, we focus on the bilayer sonophore (BLS) model of UNMOD, in which inflating intramembrane cavitations alter the membrane capacitance [31]. Previous studies have shown that the BLS-model predicts several salient features of UNMOD in the central nervous system [29], [30] (Plaksin-Shoham-Kimmel (PSK) theoretical model and the Neuronal Intramembrane Cavitation Excitation (NICE) implementation).

Unfortunately, due to computational stiffness of the PSK-model, computational studies of the BLS-model have been restricted to single-compartment point-neurons [19], [29], [30], [38], [39] and a two-compartment nanoscale model [39], leaving many important questions within the PSK-framework unanswered (e.g., importance of the spatial features of the pressure/velocity field, location of the excitation node, importance of spatially distributed membrane properties, transferability of previously obtained predictions in the point-neuron PSK-model to morphologically realistic models, etc.). As a result, the possibility to simulate the PSK-model in morphologically realistic neuron models would help to further validate the underlying assumption that central nervous system UNMOD is driven by intramembrane cavitation. Another consideration is that a multi-compartmental morphologically realistic UNMOD-model is required, in order to allow neural engineering studies of the single element focused transducer or transducer phased array, by coupling finite difference time do-

main (FDTD) ultrasound propagation [20], [40] and neuronal response simulations.

We presented preliminary results in [41] of the extension of the NICE-implementation to simulate ultrasonic neuromodulation of blue brain project cortical cells [42], [43] in the NEURON simulation environment [44], [45]. Here, computational stiffness makes extensive validation and exploration of the parameter space unfeasible within the NICE-framework, due to steep computational demands and solver instabilities. In order to improve the computational efficiency of UNMOD-simulations, a multi-scale optimized framework (SONIC) was presented by Lemaire et al. (2019), that removes the smallest timescale set by the ultrasonic frequency from the computational scheme [39]. The multi-scale approximation introduced in the SONIC-model, implies that the membrane charge and gate parameters are changing on a slow millisecond timescale. These become the state variables of the model, in terms of which the fastly changing capacitance, intramembrane gas content and transmembrane voltage are expressed. This underlying assumption is valid for point neuron-models, where membrane charge rate of change is determined by relatively small transmembrane currents. Consequently, accurate and fast integration of UNMOD is achieved with the SONIC model in point-neurons [39]. However, in morphologically-realistic multi-compartmental neurons, strong axial currents are caused by the large potential oscillations, predicted by the PSK-model [41]. These axial currents then result in fast oscillations of the membrane charge, breaking the multi-scale assumption and resulting in inaccurate integration of the multi-compartmental SONIC neuron model in terms of neuronal response and excitation threshold [46].

Fortunately, it was demonstrated in our previous study, that the fourier components of the membrane charge oscillations are changing on a slow timescale and that most of the signal energy is contained within the lowest fourier overtones [46]. These results imply that an extension of the multi-scale optimized SONIC-model is possible, by replacing the membrane charge as a slow state variable with its most important fourier components. Based on these observations, we introduce as novelty an extension of the SONIC-model for UNMOD to multi-compartmental and morphologically realistic neurons. In particular, the following innovations are being achieved in this study. First, the required number of fourier components to accurately describe the charge redistribution and voltage oscillations is determined. Second, new effective parameter tables are introduced for the voltage fourier components and protein gate rates. The dependency of voltage and rates on the ultrasonic pressure and charge oscillation amplitude is studied. Third, a computationally efficient multi-compartmental algorithm SECONIC (Spatially Extended Charge Oscillating model of Neuronal Intramembrane Cavitation) is proposed and validated in the nanoscale bilayer sonophore UNMOD model. Here, as in [46], the nanoscale two-compartmental model of the bilayer sonophore and surrounding protein islands is chosen as a test-case for the design of a computationally efficient and accurate multi-compartmental UNMOD model, as the exact solution is known by the single-compartment model due to equipotentiality [46]. Finally, computational efficiency is compared between the different PSK-models (NICE, SONIC, SECONIC) through measuring the simulation time for different ultrasonic pressures and sonophore coverage fractions.

II. Methods

The methodology of the NICE, SONIC and SECONIC models is illustrated schematically in Fig. 1. The values of the general model constants, definition of variables and functions and the membrane current dynamics, are the same as in our previous study on the importance of membrane charge oscillations in ultrasonic neuromodulation [46].

First, we briefly summarize the PSK-model for ultrasonic neuromodulation by intramembrane cavitation, in subsection II-A. For more details, we refer to previous studies of the PSK-model [19], [29]–[31], [39], [46], Second, we describe the computationally efficient algorithm SECONIC for UNMOD in multi-compartmental neuron models, that incorporates fast charge redistribution and that is based on the SONIC implementation and the PSK-model, in subsection II-B.

A. The PSK-model of UNMOD by intramembrane cavitation

The PSK-model incorporates the effect of ultrasound-induced capacitance oscillations in the Hodgkin-Huxley equations, by inclusion of the capacitive current $I_{\rm D} = V\frac{{\rm d}C_{\rm m}}{{\rm d}t}$:

$$\frac{{\rm d}Q_{\rm m}}{{\rm d}t} = C_{\rm m}\frac{{\rm d}V}{{\rm d}t} + V\frac{{\rm d}C_{\rm m}}{{\rm d}t} = \frac{I_{\rm ax}}{S_{\rm c}} - g_{\rm Na}m^3h(V-V_{\rm Na}) - g_{\rm K}n^4(V-V_{\rm K}) - g_{\rm M}p(V-V_{\rm M}) - g_{\rm l}(V-V_{\rm l}). \quad (1)$$

Here, $Q_{\rm m} = C_{\rm m}V$ is the membrane charge density, $C_{\rm m}$ the membrane capacitance and V the transmembrane voltage. $I_{\rm ax}$ is the axial current flowing into the considered compartment and $S_{\rm c}$ is the compartmental cross-sectional membrane area. As in previous studies of computational UNMOD by intramembrane cavitation [29], [30], [38], [39], [46], a regular spiking cortical Pospischil-neuron model is used [47]. The membrane conductances and Nernst-potentials of the sodium, delayed-rectifier potassium, slowly non-inactivating potassium and non-specific leak currents are given by $(g_{\rm Na}, g_{\rm K}, g_{\rm M}, g_{\rm l}) = (56, 6, 0.075, 0.0205)\ {\rm mS/cm^2}$ and $(V_{\rm Na}, V_{\rm K}, V_{\rm M}, V_{\rm l}) = (50, -90, -90, -70.3)\ {\rm mV}$, respectively. Finally, m, h, n and p are the membrane protein gating parameters for activation of transient sodium, inactivation of transient sodium, delayed-rectifier potassium and slowly non-inactivating potassium, respectively.

The membrane capacitance of the sonophore $C_{\rm BLS}$ depends on the maximal apex deflection Z (see Fig. 1):

$$C_{\rm BLS}(Z) = \frac{C_{\rm m0}\Delta}{a^2}\big[Z + \frac{a^2 - Z^2 - Z\Delta}{2Z}\ln\big(\frac{2Z+\Delta}{\Delta}\big)\big]. \quad (2)$$

Here, $a = 32\ {\rm nm}$ is the sonophore radius and $\Delta = 1.26\ {\rm nm}$ is the gap between the leaflets of the bilipid layer at rest potential. The rest capacitance is taken $C_{\rm m0} = 1\ \mu{\rm F/cm^2}$.

In this study, a nanoscale model of the bilayer sonophore (capacitance $C_{\rm BLS}$, radius a) and surrounding proteins (capacitance $C_{\rm P} \equiv C_{\rm m0}$, radius $b-a$) is considered (Fig. 1(a-b)), with partial sonophore area coverage fraction $f_{\rm BLS} = a^2/b^2$. Here,

(a) Point model

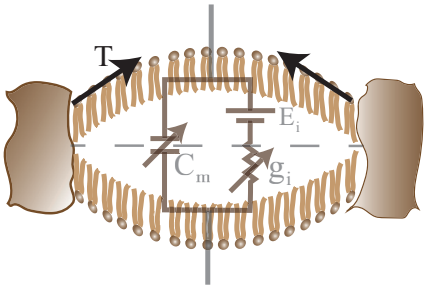

(b) Multicompartmental nanoscale model

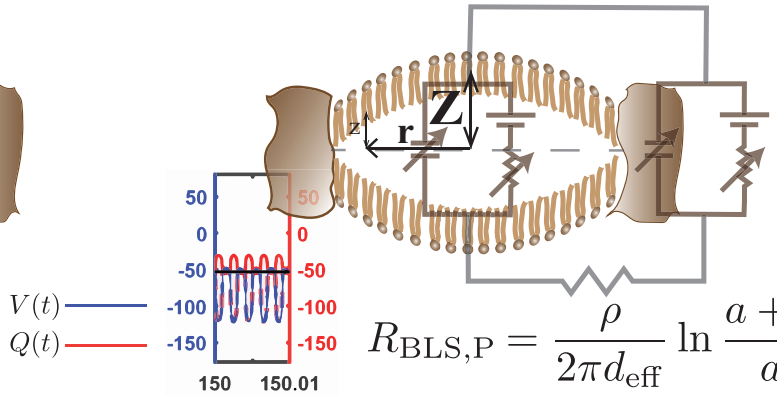

$$R_{\mathrm{BLS,P}} = \frac{\rho}{2\pi d_{\mathrm{eff}}} \ln \frac{a+b}{a}$$

(c) Pretabulation

SONIC

$$V^* = \frac{1}{T_{\mathrm{US}}} \int_0^{T_{\mathrm{US}}} \mathrm{d}t \left[\frac{Q_m}{C_m(Z)} \right]$$

$$\alpha_X^* = \frac{1}{T_{\mathrm{US}}} \int_0^{T_{\mathrm{US}}} \mathrm{d}t \left[\alpha_X \left(\frac{Q_m}{C_m(Z)} \right) \right]$$

$$\beta_X^* = \frac{1}{T_{\mathrm{US}}} \int_0^{T_{\mathrm{US}}} \mathrm{d}t \left[\beta_X \left(\frac{Q_m}{C_m(Z)} \right) \right]$$

Q_m
f_{US}
I_{US}
a_{BLS}
f_{BLS}

α_X^* β_X^* V^*

SECONIC

$$Q(t) = A_{\mathrm{Q},0} + \sum_{k=0}^{N_{\mathrm{FS}}} \left[A_{\mathrm{Q,k}} \cos(k\omega t) + B_{\mathrm{Q,k}} \sin(k\omega t) \right]$$

$$V(t) = A_{\mathrm{V},0} + \sum_{k=0}^{N_{\mathrm{FS}}} \left[A_{\mathrm{V,k}} \cos(k\omega t) + B_{\mathrm{V,k}} \sin(k\omega t) \right]$$

$A_{\mathrm{Q,k}}$
$B_{\mathrm{Q,k}}$
f_{US}
I_{US}
a_{BLS}
f_{BLS}

α_X^* $A_{\mathrm{V,k}}$ β_X^* V^* $B_{\mathrm{V,k}}$

(d)

$$\frac{\mathrm{d}Q_{\mathrm{m}}}{\mathrm{d}t} = -\sum_j g_{ax,j}(V - V_j) - \sum_i g_i(V - E_i)$$

T_{up} $C_{\mathrm{m}}(Z)$ $A_{Q,k}^{(i)}$ $B_{Q,k}^{(i)}$

NICE

$$\frac{\mathrm{d}^2 Z}{\mathrm{d}t^2} + \frac{3}{2R(Z)} \left(\frac{\mathrm{d}Z}{\mathrm{d}t} \right)^2 = \frac{1}{\rho_{\mathrm{l}} |R(Z)|} \sum_i P_i$$

SECONIC

$$A_{Q,k}^{(i)} = -\frac{1}{k\omega S_{\mathrm{k}}} \sum_{c \in C(i)} \frac{B_{\mathrm{V,k}}^{(c)} - B_{\mathrm{V,k}}^{(i)}}{R_{ic}}$$

$$B_{Q,k}^{(i)} = \frac{1}{k\omega S_{\mathrm{k}}} \sum_{c \in C(i)} \frac{A_{\mathrm{V,k}}^{(c)} - A_{\mathrm{V,k}}^{(i)}}{R_{ic}}$$

Fig. 1: Schematic overview of used models of the nanoscale bilayer sonophore. (Continued on next page.)

Fig. 1: (a) Single compartment point model. (b) Multi-compartmental nanoscale model with separate compartments for the sonophore and the protein islands. Compartments are coupled through the axial resistance $R_{\mathrm{BLS,P}}$. Membrane charge $Q(t)$ (red) and potential $V(t)$ (blue) oscillations in the sonophore (full lines) and the protein islands (dashed) are shown in the inset. (c) Pretabulation of effective potential and rate functions in the SONIC (left) and SECONIC (right) models. The SECONIC model additionally pretabulates the fourier components of the potential oscillations $A_{V,k}$ and $B_{V,k}$ (right). Independent variables of the tabulated quantities are depicted in green: SONIC tables are functions of the membrane charge Q_m, ultrasonic frequency f_{US}, intensity I_{US}, bilayer diameter a_{BLS} and coverage f_{BLS}. SECONIC independent variables additionally include the charge fourier components $A_{Q,k}$ and $B_{Q,k}$. (d) Methodology of integration of the Hodgkin-Huxley charge equation. (left, NICE-model) The membrane capacitance is continuously calculated by the Rayleigh-Plesset (RP) equation, in which the membrane charge Q_m is updated every T_{up}. (SONIC-model) Integration of the RP equation is replaced by look-up of the potential and rates. (right, SECONIC-model) The charge oscillations are determined every T_{up} by minimizing the residual of a set of algebraic equations. Subsequently, charge oscillations are used as independent variable in the SECONIC look-up tables.

b is the radius of the total model, including both the sonophore and proteins. Due to the small scale of this structure, the model is close to equipotential and a point model is accurate (Fig. 1(a)). The average membrane capacitance C_{m} is then expressed in the single-compartment point model as in [30]:

$$C_{\mathrm{m}} = f_{\mathrm{BLS}} C_{\mathrm{BLS}} + (1 - f_{\mathrm{BLS}}) C_{\mathrm{P}}. \tag{3}$$

Results of the proposed multi-compartmental scheme can now be compared with the point-model for accuracy. In the two-compartment nanoscale model (Fig. 1(b)), axial currents between the sonophore and surrounding protein islands are calculated by Ohm's law, with axial resistance between the BLS and proteins $R_{\mathrm{BLS,P}}$ (intracellular resistivity $\rho = 100\ \Omega\mathrm{cm}$ and effective depth of axial current distribution $d_{\mathrm{eff}} = 100\ \mathrm{nm}$) [39]:

$$R_{\mathrm{BLS,P}} = \frac{\rho}{2\pi d_{\mathrm{eff}}} \ln \frac{a+b}{a}. \tag{4}$$

Finally, the dynamics of the insonicated bilipid layer leaflets are described by a modified Rayleigh-Plesset equation [31]:

$$\frac{\mathrm{d}^2 Z}{\mathrm{d}t^2} + \frac{3}{2R(Z)}\Big(\frac{\mathrm{d}Z}{\mathrm{d}t}\Big)^2 = \frac{1}{\rho_{\mathrm{l}}|R(Z)|}\big[P_{\mathrm{in}} + P_{\mathrm{M}} + P_{\mathrm{ec}} - P_0 + P_{\mathrm{A}}\sin(\omega t) - P_{\mathrm{S}}(Z) - \frac{4}{|R(Z)|}\frac{\mathrm{d}Z}{\mathrm{d}t}\Big(\frac{3\delta_0\mu_{\mathrm{s}}}{|R(Z)|} + \mu_{\mathrm{l}}\Big)\big]. \tag{5}$$

Here, $\rho_{\mathrm{l}} = 1028\ \mathrm{kg/m^3}$ and $\mu_{\mathrm{l}} = 0.7 \cdot 10^{-3}\ \mathrm{Pa \cdot s}$ are the mass density and dynamic viscosity of the cerebrospinal fluid (CSF). $\mu_{\mathrm{s}} = 0.035\ \mathrm{Pa \cdot s}$ and $\delta_0 = 2\ \mathrm{nm}$ is the viscosity and thickness of the membrane leaflets. $R(Z)$ is the radius of curvature of the bilayer sonophore. The sonophore dynamics are governed by a balance of the intramembrane gas pressure P_{in}, molecular pressure P_{M}, electrostatic pressure P_{ec}, static pressure $P_0 = 10^5\ \mathrm{Pa}$, membrane tension pressure $P_{\mathrm{S}}(Z)$ and the applied ultrasonic pressure P_{A} (frequency $\omega = 2\pi f_{\mathrm{US}}$).

The gas pressure P_{in} is obtained by the ideal gas law. Here, the dynamics of the intramembrane air concentration n_{a} is determined by [29]:

$$\frac{\mathrm{d}n_{\mathrm{a}}}{\mathrm{d}t} = \frac{2S_{\mathrm{l}}(Z)D_{\mathrm{a}}}{\xi}\Big[C_{\mathrm{a}} - P_{\mathrm{in}}/k_{\mathrm{a}}\Big]. \tag{6}$$

Here, $k_{\mathrm{a}} = 1.63 \cdot 10^5\ \mathrm{Pa \cdot m^3/mol}$, $D_{\mathrm{a}} = 3 \cdot 10^{-9}\ \mathrm{m^2/s}$ and $C_{\mathrm{a}} = 0.62\ \mathrm{mM}$ are respectively the Henry constant, diffusion coefficient and molar concentration of air in CSF. $S_{\mathrm{l}}(Z)$ is the effective area of a single leaflet and $\xi = 0.5\ \mathrm{nm}$ is the thickness of the diffusion boundary layer.

In the NICE-implementation [29], the computational efficiency is improved by decoupling the Rayleigh-Plesset equation and the Hodgkin-Huxley charge equation by introducing an update time T_{up} (Fig. 1(d)). In order to further reduce the model stiffness, multiscale optimization in the SONIC model [39] consists of pretabulation the effective membrane voltage and rates (Fig. 1(c)), e.g., for the membrane voltage ($T_{\mathrm{US}} = 1/f_{\mathrm{US}}$):

$$V^* = \frac{1}{T_{\mathrm{US}}}\int_0^{T_{\mathrm{US}}} \frac{Q_{\mathrm{m}}}{C_{\mathrm{m}}(Z(t))}\mathrm{d}t. \tag{7}$$

The SONIC-tables for the effective membrane potential V^* and rate functions α_X^* and β_X^* (Fig. 1(c)) are then interpolated, while solving the modified Hodgkin-Huxley equation (Fig. 1(d)).

The Rayleigh-Plesset and electrodynamical equation are solved by the Matlab® Variable Step Variable Order (VSVO) ode-solvers [48], [49]: ode113 (order 1-13, Adams-Bashort-Moulton predictor-corrector pairs), ode23t (order 2-3, trapezoidal rule), and ode15s (stiff VSVO-solver, order 1-5, based on numerical differentiation formulas). Table I summarizes the used integration methods in the NICE, SONIC and SECONIC models, including the maximal timestep $\mathrm{d}t_{\max}$, absolute tolerances (Abs. Tol.) and relative tolerances (Rel. Tol.).

TABLE I: Summary of integration methods

	NICE	SONIC	SECONIC
T_{up}	25 μs	–	50 μs
Rayleigh-Plesset solver			
Solver	ode113	ode113/ode23t	
Abs. Tol. (Z,$\mathrm{d}Z/\mathrm{d}t$, n_{a})	(0.1 pm, 1 fm/μs, 10^{-24} mole)		
Rel. tol.	0.0001		
$\mathrm{d}t_{\max}$	$0.025/f_{\mathrm{US}}$		
Point model (electrodynamics solver)			
Solver	ode113		–
Abs. Tol. (V, gates)	(1 μV, 0.001)		–
Rel. Tol.	0.001		–
$\mathrm{d}t_{\max}$	$0.025/f_{\mathrm{US}}$	50 μs	–
Multi-compartmental model (electrodynamics solver)			
Solver	ode15s		
Abs. Tol. (V, gates)	(0.1 nV, 10^{-7})		
Rel. Tol.	0.0001		
$\mathrm{d}t_{\max}$	$0.025/f_{\mathrm{US}}$	50 μs	

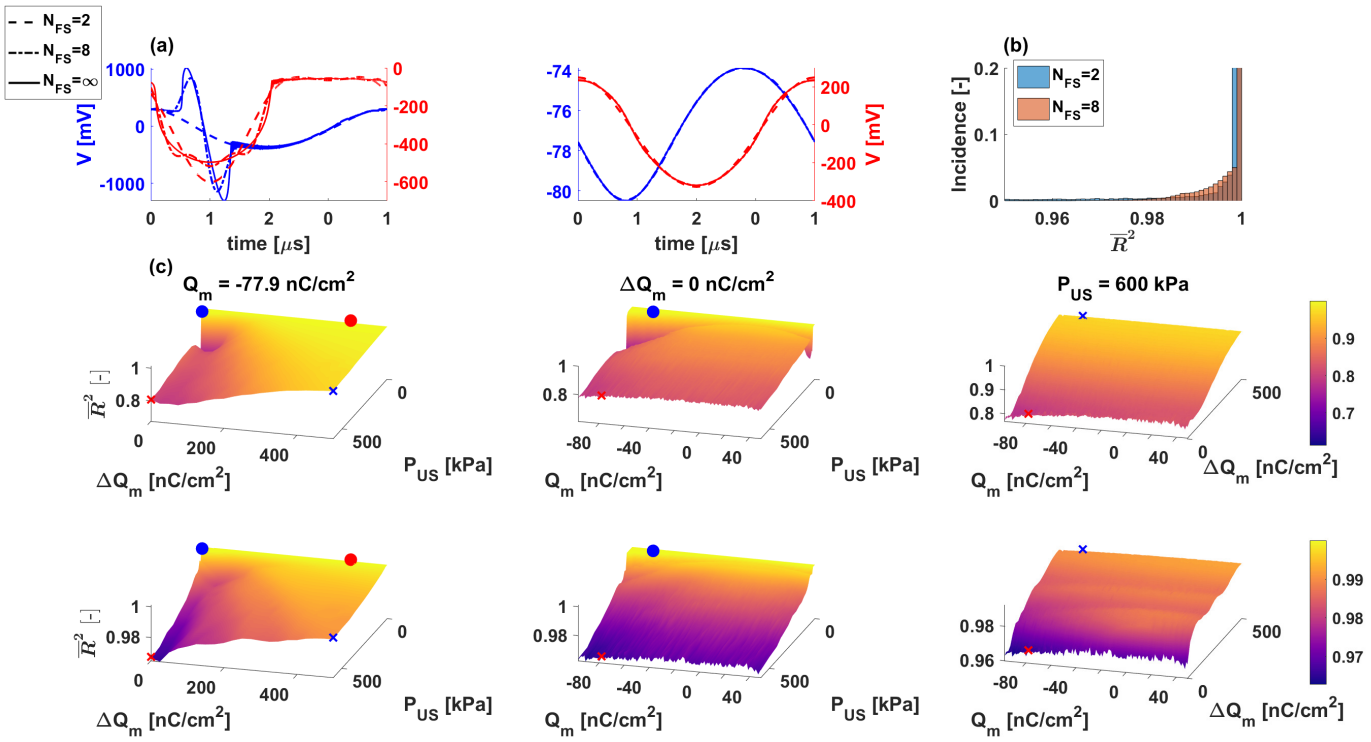

Fig. 2: Goodness of fit (quantified by $\overline{R}^2$) to the transmembrane voltage V for two and eight fourier series components N_{FS}, as function of membrane charge, charge oscillation amplitude and ultrasonic pressure. Full lines represent the numerical solution ($N_{\mathrm{FS}} = \infty$). (a) Examples of fourier fits with lower and higher $\overline{R}^2$ (left and right, respectively). (b) Histogram of incidence of $\overline{R}^2$ for two and eight fourier components. (c) Goodness of fit surfaces as function of charge oscillation amplitude ΔQ_{m}, membrane charge Q_{m} and pressure amplitude P_{US} for $N_{\mathrm{FS}} = 2$ (first row) and $N_{\mathrm{FS}} = 8$ (second row). The markers indicate the example fits of (a) (crosses for (a)(left) and circles for (a)(right), corresponding colour).

B. Computationally efficient multi-compartmental algorithm for morphologically realistic neurons (SECONIC)

In view of the importance of charge redistribution and fast oscillations for an accurate multi-compartmental UNMOD model, fourier series are used to describe the local charge per compartment:

$$Q(t) = A_{\mathrm{Q},0} + \sum_{k=1}^{N_{\mathrm{FS}}} \left[A_{\mathrm{Q,k}} \cos(k\omega t) + B_{\mathrm{Q,k}} \sin(k\omega t)\right] = A_{\mathrm{Q},0} + \sum_{k=1}^{N_{\mathrm{FS}}} \left[Q_k \cos(k\omega t + \phi_k)\right]. \quad (8)$$

Here, $A_{\mathrm{Q,k}}$ and $B_{\mathrm{Q,k}}$ are fourier components ($Q_k = \sqrt{A_{\mathrm{Q,k}}^2 + B_{\mathrm{Q,k}}^2}$ and $\phi_k = -\operatorname{atan2}(B_{\mathrm{Q,k}}, A_{\mathrm{Q,k}})$) and N_{FS} is the number of fourier series overtones. With similar notation for the membrane voltage:

$$V(t) = A_{\mathrm{V},0} + \sum_{k=1}^{N_{\mathrm{FS}}} \left[A_{\mathrm{V,k}} \cos(k\omega t) + B_{\mathrm{V,k}} \sin(k\omega t)\right] = A_{\mathrm{V},0} + \sum_{k=1}^{N_{\mathrm{FS}}} \left[V_k \cos(k\omega t + \psi_k)\right]. \quad (9)$$

Effective parameters can now be defined by solution of the Rayleigh-Plesset equation until periodicity for the rate functions α_X^*, β_X^* (in this study, $X \in \{m, n, h, p\}$: $N_g = 4$ gate parameters) and the membrane voltage ($A_{V,0} = V_{\mathrm{eff}}$, V_k, ψ_k; with $k = 1 \ldots N_{\mathrm{FS}}$). Consequently, pretabulation of the effective parameters consists of the calculation of $2N_{\mathrm{g}} + 2N_{\mathrm{FS}} + 1$ look-up tables ($\big(2N_{\mathrm{FS}}{+}5\big)$-dimensional: independent variables are the ultrasonic frequency f_{US}, the intensity I_{US}, the bilayer sonophore diameter a_{BLS} and coverage f_{BLS}, and the charge fourier components ($A_{\mathrm{Q,k}}$, ϕ_k, with $k = 1 \ldots N_{\mathrm{FS}}$ and $A_{\mathrm{Q},0}$), cfr. Fig. 1). Note that the charge oscillation phases ϕ_k are relative w.r.t. the phase of the ultrasonic pressure sine in (5): it is not possible to set one of these phases ϕ_k to zero by convention (making use of time invariance).

In this study, SECONIC-tables sample each charge oscillation amplitude with step 25 $\mathrm{nC/cm^2}$ (0 $\mathrm{nC/cm^2}$ to 100 $\mathrm{nC/cm^2}$) and the oscillation phase with step $2\pi/9$. Charge oscillation amplitudes and phases are upsampled fourfold and twice, respectively, with modified Akima interpolation [50], [51] (see also section IV). The membrane charge dimension $A_{\mathrm{Q},0}$ is sampled with step 5 $\mathrm{nC/cm^2}$ ($Q_{\mathrm{m}0} - 25$ $\mathrm{nC/cm^2}$ to 50 $\mathrm{nC/cm^2}$)

In addition to currents caused by the effective membrane voltage, oscillatory axial currents ΔI_{ax} are driven by the

voltage oscillations:

$$\Delta I_{\mathrm{ax}}^{(i)} = \sum_{k=1}^{N_{\mathrm{FS}}} \sum_{c\in C(i)} \frac{V_{\mathrm{k}}^{(c)} \cos(k\omega t + \psi_k^{(c)})}{R_{ic}} - \frac{V_{\mathrm{k}}^{(i)} \cos(k\omega t + \psi_k^{(i)})}{R_{ic}}. \quad (10)$$

Superscripts refer to the compartment or segment index, R_{ic} is the axial compartmental resistance between segment i and c, and $C(i)$ is the set of compartments that are connected with segment i.

Because of the conditional linearity in the membrane voltage of the equation $\mathrm{d}Q/\mathrm{d}t = I_{\mathrm{ax}}/S_{\mathrm{c}}^{(i)} - \sum_l g_l(V - E_l)$, we can calculate the charge oscillation by:

$$Q_k^{(i)} e^{j\phi_k^{(i)}} = \frac{1}{jk\omega S_{\mathrm{c}}^{(i)}} \sum_{c\in C(i)} \frac{V_{\mathrm{k}}^{(c)} e^{j\psi_k^{(c)}} - V_{\mathrm{k}}^{(i)} e^{j\psi_k^{(i)}}}{R_{ic}}. \quad (11)$$

Or equivalently,

$$A_{Q,k}^{(i)} = -\frac{1}{k\omega S_{\mathrm{c}}^{(i)}} \sum_{c\in C(i)} \frac{B_{V,\mathrm{k}}^{(c)} - B_{V,\mathrm{k}}^{(i)}}{R_{ic}}. \quad (12)$$

$$B_{Q,k}^{(i)} = \frac{1}{k\omega S_{\mathrm{c}}^{(i)}} \sum_{c\in C(i)} \frac{A_{\mathrm{V,k}}^{(c)} - A_{V,\mathrm{k}}^{(i)}}{R_{ic}} \quad (13)$$

Here, the right hand side is dependent on Q_k and ϕ_k, through the look-up tables of V_k and ψ_k. The norm of the vector with the residuals of (12)–(13) is minimized every $T_{\mathrm{up}} = 50$ μs by the Matlab® fminsearch-function (simplex search method, [52]).

In the specific case of the nanoscale two-compartment model of the bilayer sonophore and surrounding proteins, we have $S_{\mathrm{BLS}} = \pi a^2$ and $S_{\mathrm{P}} = [(1 - f_{\mathrm{BLS}})/f_{\mathrm{BLS}}]S_{\mathrm{BLS}}$. Consequently, $Q_{\mathrm{BLS}} = -[(1 - f_{\mathrm{BLS}})/f_{\mathrm{BLS}}]Q_{\mathrm{P}}$ and $\phi_{\mathrm{BLS}} = \phi_{\mathrm{P}}$ (or equivalently, $A_{Q,\mathrm{BLS}} = -[(1 - f_{\mathrm{BLS}})/f_{\mathrm{BLS}}]A_{Q,\mathrm{P}}$ and $B_{Q,\mathrm{BLS}} = -[(1 - f_{\mathrm{BLS}})/f_{\mathrm{BLS}}]B_{Q,\mathrm{P}}$), reducing (11) to a set of N_{FS} complex equations.

III. Results

A. Goodness of fit and extension of effective parameters

In [46], we have shown that although the membrane charge oscillates on a microsecond timescale set by the ultrasonic frequency, the corresponding fourier series components vary

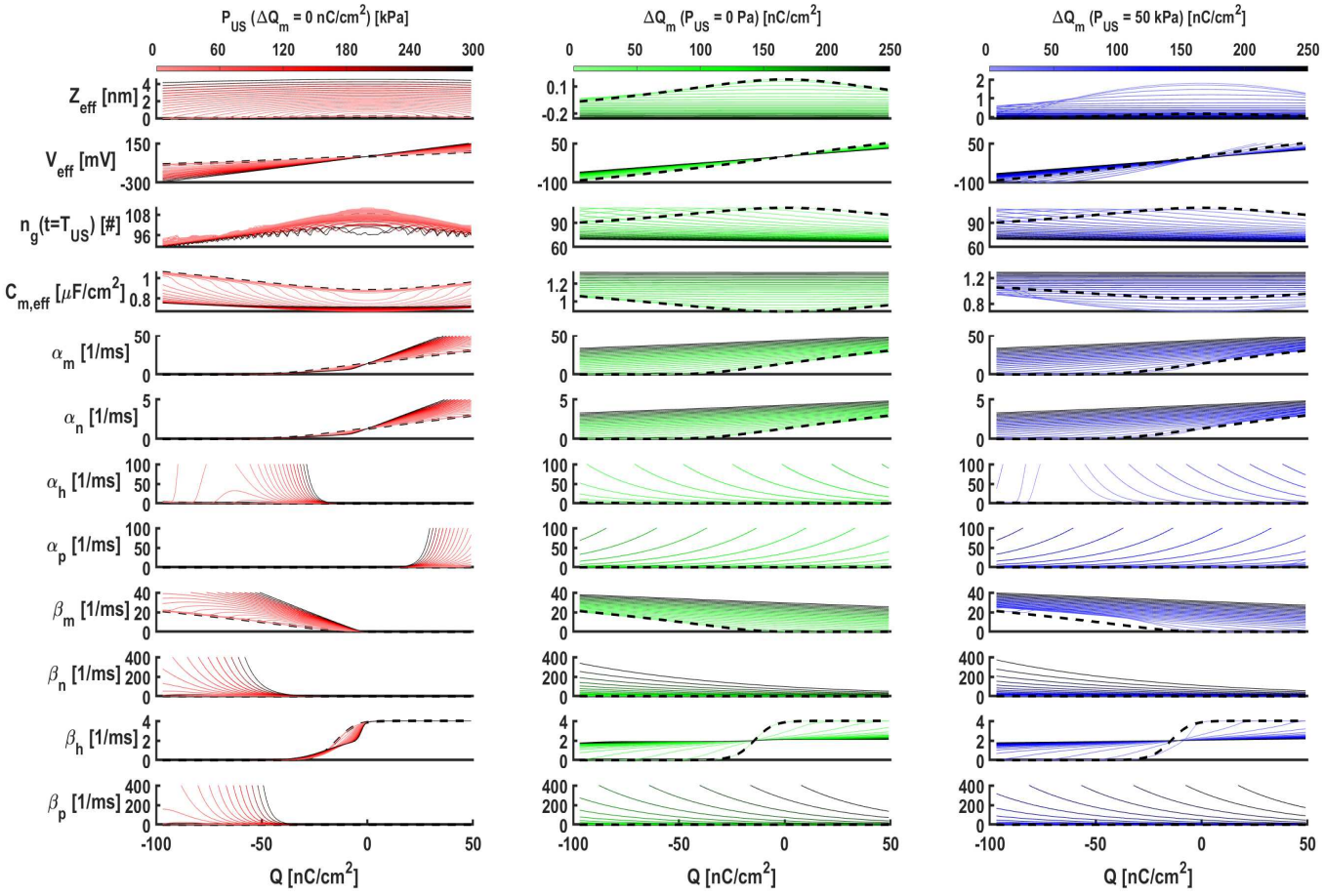

Fig. 3: Dependency of effective SECONIC-parameters on charge and ultrasound oscillations. Effective displacement Z^*, membrane potential V^*, intramembrane gas particles n_{g}, membrane capacitance $C_{\mathrm{m,eff}}$ and rate parameters as function of membrane charge for different ultrasonic pressure levels at $\Delta Q_m = 0$ nC/cm^2 (left) and as function of different membrane charge oscillation amplitudes at $P_{\mathrm{US}} = 0$ Pa (middle) and at $P_{\mathrm{US}} = 50$ kPa (right). The applied charge oscillation is a pure cosine (i.e., $Q_{\mathrm{k}} = 0$ $(k > 1)$ and $\forall k$: $\phi_k = 0$), with $Q = A_{\mathrm{Q,0}}$ and $\Delta Q_{\mathrm{m}} = Q_1$.

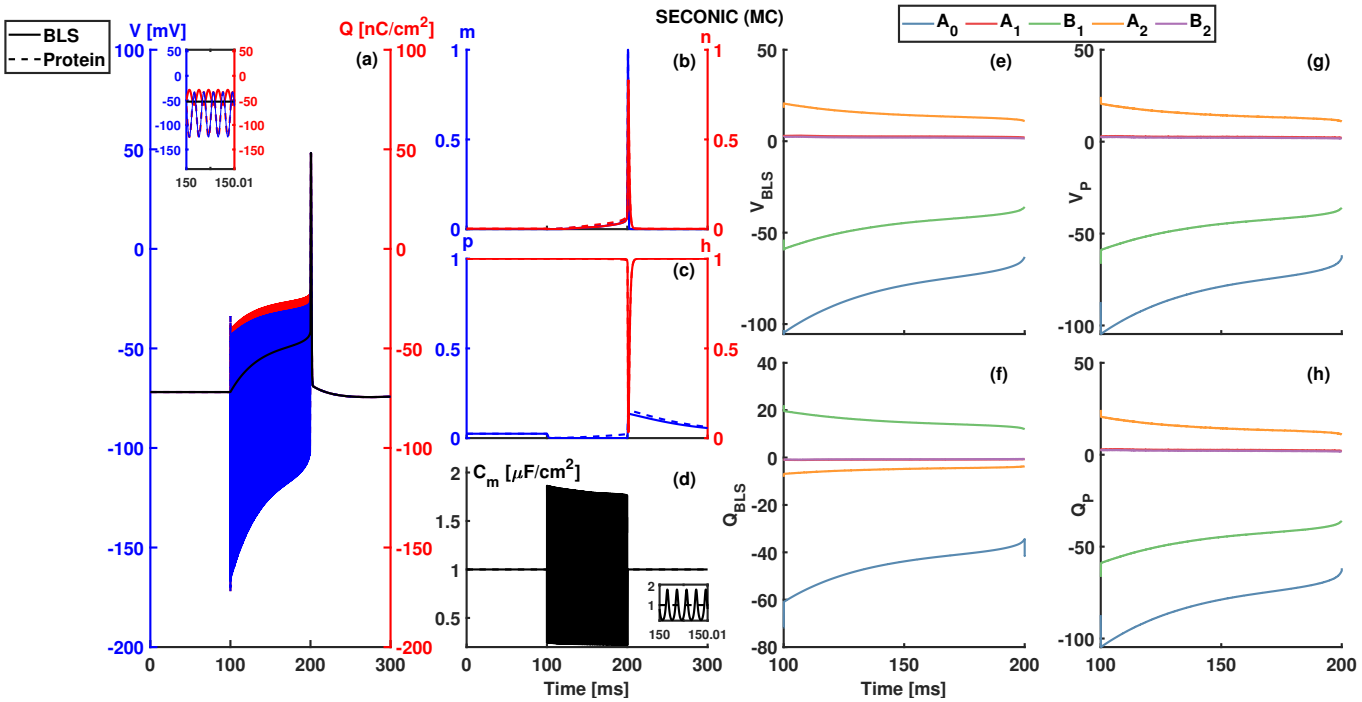

Fig. 4: Detailed illustration of the neuronal response to UNMOD in the SECONIC-model. Insonication of regular spiking neuron (continuous wave ultrasound, pulse onset and pulse duration set to 100 ms, $P_{\mathrm{US}} = 100\,\mathrm{kPa}$ ($I_{\mathrm{sp}} = 321\,\mathrm{mW/cm^2}$)) with partial sonophore coverage ($f_{\mathrm{BLS}} = 0.75$, $a_{\mathrm{BLS}} = 32\,\mathrm{nm}$). Two compartments are used to model the bilayer sonophore (full lines) and the surrounding protein islands (dashed lines). (a) Membrane charge (red) and voltage (blue) trace. The total membrane charge per surface area is depicted in black. Charge and voltage oscillations are visible in the inset. (b-c) gate parameter traces (m, n, h, and p)); (d) membrane capacitance plots. (e-h) Temporal dynamics of effective values and first two overtones of the membrane potential (e-g) and charge (f-h) at the bilayer sonophore level (e,f) and the protein islands (g,h).

on a slower millisecond timescale. Indeed, fourier overtone components are determined by the set of equations (12)–(13), the solution of which is dependent on the ultrasonic waveform, the sonophore parameters and the effective (time-averaged) membrane charge. Here, the effective membrane charge density, determined by the time-averaged Hodgkin-Huxley equation in Fig. 1(d), will be changing on a slow millisecond timescale. Consequently, the overtone components are expected to follow this millisecond timescale as well. Furthermore, as expected, most of the signal energy of the charge and voltage traces are contained within the lowest overtone numbers [46]. These observations are the basis of the SECONIC-model, which includes a limited number of fourier components in order to account for the ultrasound-induced charge redistribution between compartments.

To determine the required number of fourier series components and to improve our understanding of the expected accuracy of the SECONIC solver for different ultrasonic waveforms, we study the goodness of the non-linear least squares fourier series fit to the membrane voltage in Fig. 2. The goodness-of-fit is quantified by the adjusted R-squared $\overline{R}^2 = 1 - (1 - R^2)\frac{N_{\mathrm{s}}-1}{N_{\mathrm{s}}-2N_{\mathrm{FS}}-1}$, with N_{s} the number of sample points in the potential trace. The metric $\overline{R}^2$ is mostly used in statistics, but its definition is also useful here to quantify the goodness-of-fit of a predictive model without statistical basis. Here, $R^2 = 1 - \mathrm{SSE}/\mathrm{SS}_{\mathrm{tot}}$ (SSE is the sum of squared errors between the fit and the voltage trace, $\mathrm{SS}_{\mathrm{tot}}$ is the squared sum of the samples of the voltage trace) can be interpreted as the fraction of signal energy of the voltage trace that can be explained by the fourier series fit. R^2 will automatically increase with N_{FS}, while $\overline{R}^2$ corrects for overfitting and as a result gives a better measure of how many fourier series components should be taken into account. The best goodness of fit is obtained for small ultrasonic intensities, regardless of the charge oscillation amplitude (Fig. 2(a)(right)). Conversely, the adjusted R-squared value decreases for increasing intensities (Fig. 2(left)), due to the non-linear relation between the membrane voltage and the ultrasonic pressure (through the Rayleigh-plesset equation (5) and membrane capacitance formula (2)). For eight fourier series components $N_{\mathrm{FS}} = 8$ (Fig. 2(c)(lower row),(b)), very good fits are obtained (minimum, mean and standard deviation of $\overline{R}^2$ is 0.96, 0.9976 and 0.0047, respectively). Furthermore, also for $N_{\mathrm{FS}} = 2$ (Fig. 2(c)(upper row),(b)), satisfactory fits are obtained with minimum, mean and standard deviation of $\overline{R}^2$ equal to 0.61, 0.98, and 0.0412. As mentioned, the lowest $\overline{R}^2$ values are due to very high ultrasonic pressures. Consequently, the best performance of the SECONIC model is expected at low ultrasonic pressures, especially for lower numbers of considered fourier series components N_{FS}.

The overtone fourier components that describe the membrane charge oscillations will influence the neuronal dynamics

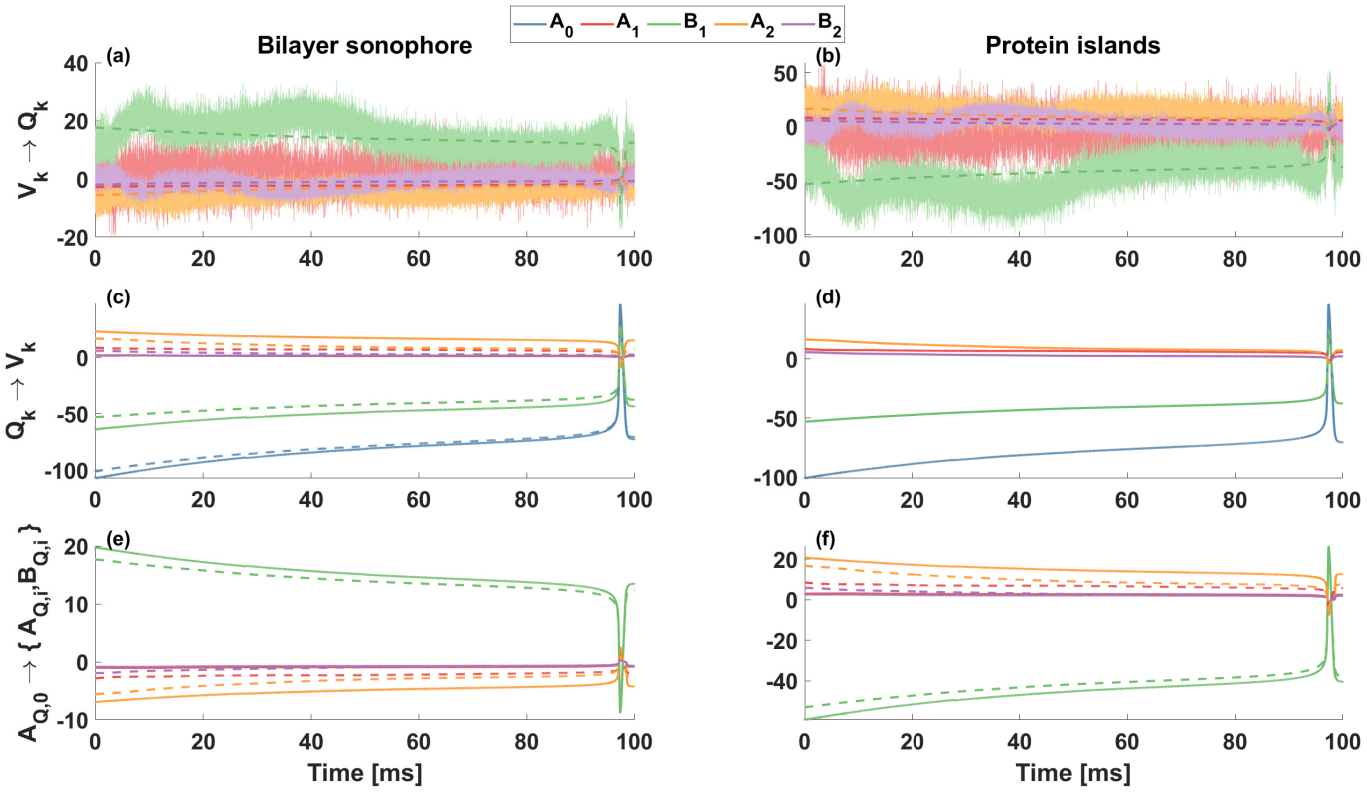

Fig. 5: Analysis of numerical errors in SECONIC by hybrid NICE-MC and SECONIC simulations in the nanoscale multi-compartmental model. Insonication of regular spiking neuron (continuous wave ultrasound, pulse onset and pulse duration set to 100 ms, $P_{\mathrm{US}} = 100\,\mathrm{kPa}$ ($I_{\mathrm{sp}} = 321\,\mathrm{mW/cm^2}$)) with partial sonophore coverage ($f_{\mathrm{BLS}} = 0.75$, $a_{\mathrm{BLS}} = 32\,\mathrm{nm}$). The effective value and first two overtones of the membrane charge (top, bottom) and the membrane voltage (middle) are determined for the NICE-MC model (dashed lines: $Q_{\mathrm{k}}^{\mathrm{NICE,MC}}$ and $V_{\mathrm{k}}^{\mathrm{NICE,MC}}$ obtained from the NICE-MC solution $Q_{\mathrm{NICE,MC}}(t)$ and $V_{\mathrm{NICE,MC}}(t)$) in the bilayer sonophore compartment (left) and the protein islands (right). By the SECONIC formulation, charge fourier components Q_{k} are derived from the NICE-MC voltage fourier components V_{k} ($V_{\mathrm{k}}^{\mathrm{NICE,MC}} \to Q_{\mathrm{k}}$, top) and from the NICE-MC effective charge component ($A_{\mathrm{Q},0}^{\mathrm{NICE,MC}} \to \{A_{\mathrm{Q,i}}, B_{\mathrm{Q,i}}\}$, bottom). Similarly, voltage fourier components V_{k} are derived from NICE-MC charge fourier components Q_{k} ($Q_{\mathrm{k}}^{\mathrm{NICE,MC}} \to V_{\mathrm{k}}$, middle). Here, the arrow-symbol ($\to$) should be interpreted as the action of the SECONIC-model: $X \to Y \triangleq X^{\mathrm{NICE,MC}} \xrightarrow{SECONIC} Y$.

in (1) (Fig. 1(d)), indirectly via their influence on the effective potential and rate functions. This is investigated in Fig. 3, where the effective rate parameters, displacement, membrane voltage, capacitance, and intramembrane gas content are shown as function of the oscillation amplitude and ultrasonic pressure. We observe that larger charge oscillations imply a stronger electrostatic interaction. As a consequence, effective displacement and membrane voltage are inversely proportional to the amplitude of the charge oscillation. Thus, ultrasonic pressure and membrane charge oscillation amplitude have opposing influence on the membrane capacitance and effective potential (cfr. different columns in Fig. 3). However, the effect of ultrasonic intensity and oscillation amplitude on the rate functions is similar, via the proportionality between voltage and charge oscillations. Here, also the order of magnitude of the influence of charge oscillation amplitude and ultrasonic pressure on the rate functions is comparable.

B. SECONIC: accuracy in the nanoscale BLS-protein model

Fig. 4(a-d) shows the neuronal response for insonication with $I_{\mathrm{sp}} = 321\,\mathrm{mW/cm^2}$ (i.e., $P_{\mathrm{US}} = 100\,\mathrm{kPa}$; $f_{\mathrm{BLS}} = 0.75$, $a_{\mathrm{BLS}} = 32\,\mathrm{nm}$) in the SECONIC model with $N_{\mathrm{FS}} = 2$. This case could be compared with the results for the NICE and SONIC model in [46](Figs. 2–3). The predicted neuronal response in the SECONIC model is similar to the results obtained by the NICE model or SONIC single-compartment model. In particular, both the SECONIC multi-compartmental and SONIC single-compartment model predict a single action potential at the end of the stimulation duration. In contrast to the SONIC-MC model, no repetitive spiking response is observed for this insonication case in the SECONIC-MC model, implying that SECONIC is accurately taking into account fast charge redistribution. Furthermore, the temporal evolution of the effective values and first two overtones of the membrane voltage and charge in the SECONIC model (Fig. 4(e-h)) demonstrate qualitatively similar trends as the results predicted by the NICE-MC model (dashed lines, Fig. 5).

However, some deviations between the SECONIC and

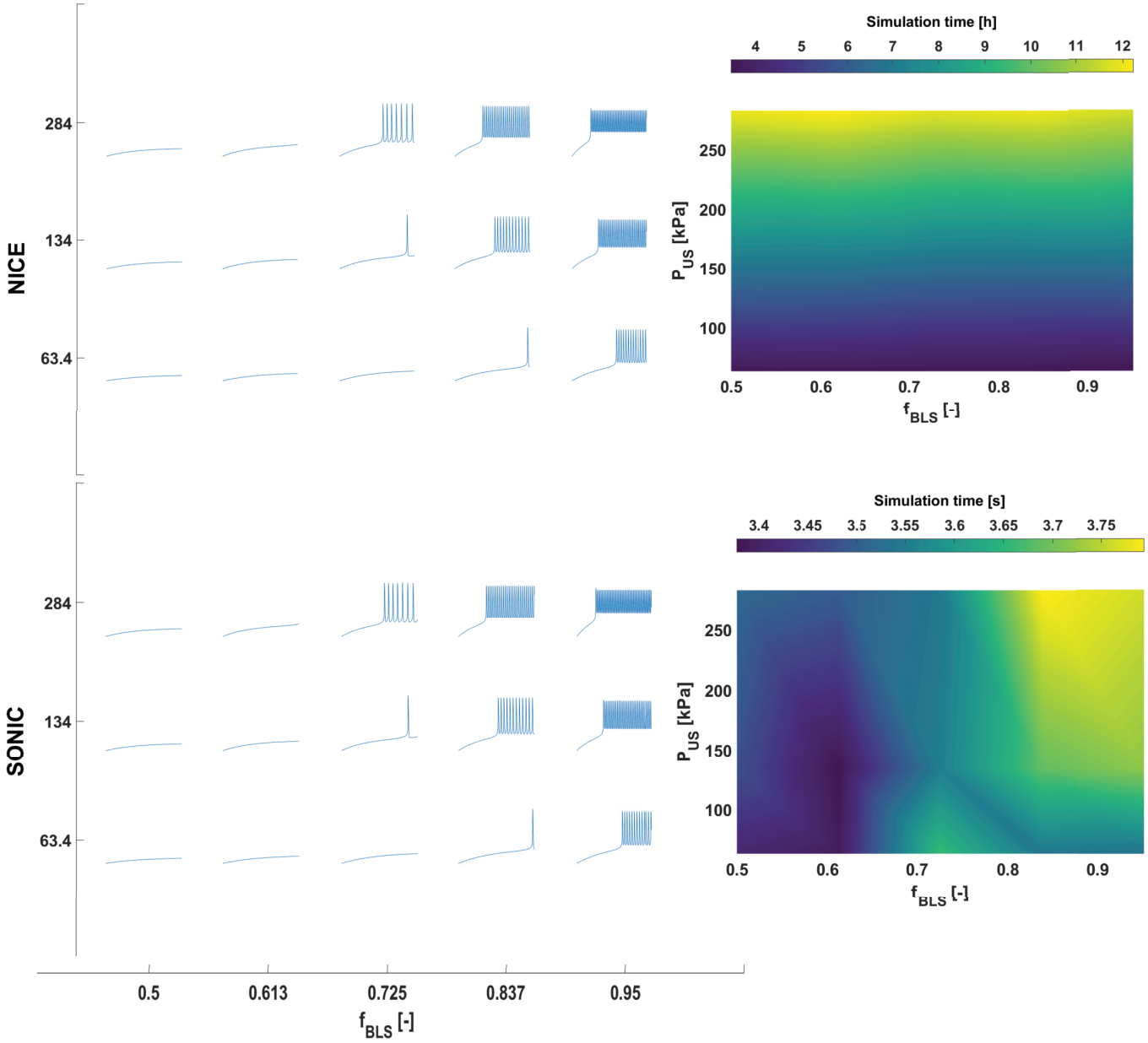

Fig. 6: Accuracy and computational efficiency of the NICE and SONIC point-neuron models. Response of regular spiking neuron ($f_{\mathrm{US}} = 500$ kHz) for different insonication intensities and sonophore coverage f_{BLS} (left; total membrane charge trace) and corresponding simulation time (right) for the NICE (top) and SONIC (bottom) point-neuron model.

NICE model responses are observed. Most importantly, the SECONIC bilayer sonophore voltage-oscillations reach more depolarized values compared to NICE. Consequently, the membrane capacitance oscillation also extends to larger values in the SECONIC model. These discrepancies can likely be explained by the limited number of fourier components ($N_{\mathrm{FS}} = 2$) in combination with insufficient sampling of the independent variables of the SECONIC-table (see section IV).

To better understand where numerical errors can emerge in the workflow of the SECONIC model, an intermediary result is shown in Fig. 5. Here, as a benchmark, voltage and charge fourier components are determined from the NICE-MC simulation results. In Fig. 5(a-b) the charge fourier components are determined within the SECONIC framework ((12) –(13)) from the NICE-MC voltage components V_{k}. Here, the calculated charge components ($V_{\mathrm{k}} \rightarrow Q_{\mathrm{k}}$; full lines) follow the expected NICE-MC components (Q_{k}; dashed lines). There is significant noise on the charge components that are calculated from the corresponding voltage components ($V_{\mathrm{k}} \rightarrow Q_{\mathrm{k}}$), both in the bilayer sonophore and protein islands (Fig. 5(a) and Fig. 5(b), respectively). This can be explained by the fact that the charge oscillations components are derived from the potential difference between both compartments: as the bilayer sonophore and protein islands are close to equipotential, this potential difference is almost zero and susceptible to small numerical errors in the determination of the fourier components or in the

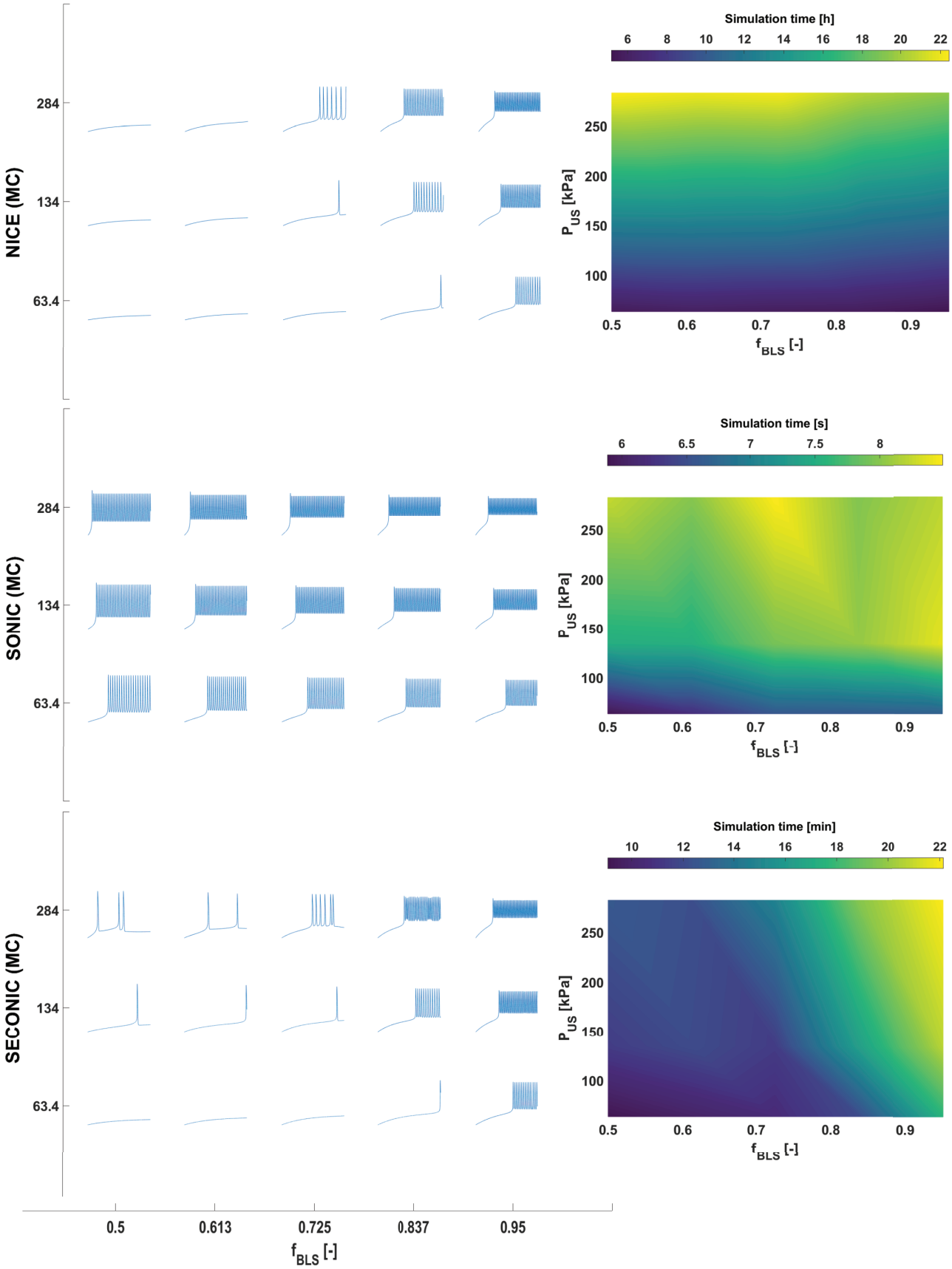

Fig. 7: Accuracy and computational efficiency of the NICE, SONIC and SECONIC nanoscale multi-compartmental models. Response of regular spiking neuron ($f_{\mathrm{US}} = 500$ kHz) for different insonication intensities and sonophore coverage f_{BLS} (left; total membrane charge trace) and corresponding simulation time (right) for the NICE (top), SONIC (middle), and the SECONIC (bottom; $N_{\mathrm{FS}} = 2$) nanoscale multi-compartmental model.

NICE-MC solution. In Fig. 5(c-d) the voltage fourier components are determined by look-up in the SECONIC-tables of the NICE-MC charge components Q_{k} ($Q_{\mathrm{k}} \rightarrow V_{\mathrm{k}}$; dashed lines). A small deviation is seen from the expected NICE-MC voltage components V_{k}, explained by errors due to the restricted number of considered fourier components (here, $N_{\mathrm{FS}} = 2$) and interpolation errors (dependent on the sampling resolution, interpolation method and upsampling method). Note, that there is no error on the voltage components $Q_{\mathrm{k}} \rightarrow V_{\mathrm{k}}$ in the protein island compartment (in Fig. 5(d), the components $Q_{\mathrm{k}} \rightarrow V_{\mathrm{k}}$ (full) and V_{k} (dashed) coincide). Indeed, in the protein island compartment, the capacitance is constant $C_{\mathrm{m}}(t) \equiv C_{\mathrm{m0}}$ and voltage component look-up is exact. Finally, in Fig. 5(e)-(f) charge components are calculated from the zeroth order NICE-MC charge ($A_{\mathrm{Q},0} \rightarrow Q_{\mathrm{k}}$; full lines) by minimisation of the residual of the SECONIC-equations (12)–(13), supplemented with the look-up tables. Comparison with the predicted NICE-MC solution (Q_{k} dashed lines) demonstrates a similar error as for the voltage component look-up $Q_{\mathrm{k}} \rightarrow V_{\mathrm{k}}$ in Fig. 5(c-d). Solving the SECONIC-equations ((12)–(13)) corresponds with finding a self-consistent solution for the charge oscillations. The accuracy of this solution is only dependent on the number of considered fourier components N_{FS} and the interpolation of the SECONIC look-up tables. The SECONIC charge oscillation solution ($A_{\mathrm{Q},0} \rightarrow Q_{\mathrm{k}}$; Fig. 5(e-f)) does not depend on small numerical errors that arise in the NICE-MC solution or in the calculation of the fourier components Q_{k} and V_{k}: consequently, the observed noise in the intermediate result $V_{\mathrm{k}} \rightarrow Q_{\mathrm{k}}$ (Fig. 5(a-b)) is not present in the final charge oscillation SECONIC-solution $A_{\mathrm{Q},0} \rightarrow Q_{\mathrm{k}}$ (Fig. 5(e-f)).

C. SECONIC: Simulation efficiency in the BLS-Protein model

In this section, we compare the required simulation time for insonication during $100\ \mathrm{ms}$ between the SONIC, SECONIC and NICE single and multi-compartmental models. Results are shown in Fig. 6 (point-model) and Fig. 7 (nanoscale multi-compartmental model): simulations are performed on a 20 core server (2.2 GHz clock rate, 192 GB RAM). Simulation times of the faster SONIC and SECONIC models are averaged over 10 trials. These simulation times per $100\ \mathrm{ms}$ insonication are meant as a rough measure of computational efficiency.

First, in the NICE model the required simulation time increases with ultrasonic intensity, independent of the neuronal response. In contrast, simulation time in the SONIC and SECONIC models reflects the neuronal activity. As observed by [39], this is explained by the fact that the computational complexity of the NICE model is determined at the timescale set by the ultrasonic period. Consequently, neuronal activity will hardly affect the computational stiffness in the NICE-model, while increased stiffness in the equation set is caused by the larger leaflet displacements at higher pressures. However, in the SONIC and SECONIC model, neuronal stiffness is not influenced by the increased leaflet deflection, but by increased neuronal activity via the variable-step differential solvers.

Second, the simulation time per $100\ \mathrm{ms}$ insonication is in the order of hours and seconds for NICE and SONIC, respectively. In both frameworks, the walltime for the two-compartment model is slightly lower than twice the simulation time of the single-compartment model. Walltimes are in the order of minutes for the SECONIC model.

Third, as discussed earlier, the single- and multi-compartmental NICE model and the single-compartment SONIC model yield similar neuronal response results (cfr. Fig. 6 and Fig. 7). This indicates that a single-compartment model is sufficient for the nanoscale bilayer sonophore and that SONIC is an accurate and efficient implementation of single-compartment UNMOD models. However, the SONIC implementation applied to the two-compartment model (SONIC (MC); Fig. 7) is inaccurate, especially for sonophore coverage f_{BLS} closer to 0.5. The SONIC model does not take into account fast charge oscillations caused by strong axial currents in multi-compartmental models. Here, the SECONIC model (SECONIC (MC), Fig. 7) takes into account these charge oscillations. For two fourier components ($N_{\mathrm{FS}} = 2$) and with the used sampling, predicted neuronal response is accurate if the applied ultrasonic intensity is not too high. For higher pressures $P_{\mathrm{US}} > 100\ \mathrm{kPa}$ ($I_{\mathrm{spta}} > 321\ \mathrm{mW/cm^2}$), the quality of the simulation results starts to decrease with the ultrasonic intensity. This is expected as also the goodness of the fourier series fit to the voltage trace decreases with ultrasonic intensity (cfr. Fig. 2).

IV. Discussion

The PSK-UNMOD model and its potential generalization to multi-compartmental models is investigated, resulting in the SECONIC-model that includes fast charge redistribution between compartments in the multi-scale optimized scheme. The SECONIC-model is a step in the direction of morphologically realistic UNMOD models.

In this study, the SECONIC framework is tested and compared with the NICE and SONIC models in the nanoscale model of the BLS-Protein structure, also investigated in [39], [46]. Due to the small spatial scale, the considered model can be assumed to be close to equipotential, implying that results of multi-compartmental models have to reproduce the single-compartment solution. Consequently, this nanoscale BLS-Protein model is ideally suited for the first design of an accurate and computationally efficient multi-compartmental scheme, because the exact solution is known by the point-model approximation, thus allowing us to assess the accuracy of the SECONIC-simulations. We note that fast charge redistribution in this nanoscale model is also relevant for larger morphologically realistic neurons. Indeed, we found charge oscillations with amplitude in the order of $60\ \mathrm{nC/cm^2}$, upon application of a sinusoidal capacitance oscillation (amplitude equal to 80% of the local capacitance) in a blue brain project cortical cell [42], [43]. The amplitude of the charge oscillation is expected to depend on the interplay of several factors, such as the ultrasonic waveform, the axial resistance between compartments, the compartmental membrane area… Here, further studies will be necessary, to determine the required number of fourier components N_{FS} in the SECONIC-model at different locations of the morphologically realistic neuron

for a given ultrasonic stimulus waveform, which is expected to depend also on the local amplitude of the charge oscillation.

A. Voltage and charge fourier series components - accuracy

The first consideration during the construction of the SECONIC-model, is the number of fourier series components N_{FS} that should be included in the multi-scale optimized scheme. Furthermore, it would be interesting to know how the required N_{FS}, or conversely the accuracy of SECONIC, depends on the applied ultrasonic waveform and the expected charge oscillation amplitude. This is investigated by means of the fourier series goodness of fit, quantified by the adjusted R^2 value. The goodness of fit is high for two fourier components (mean $\overline{R}^2_{\mathrm{FS}=2} = 0.98$, standard deviation 0.0412), although outliers with weaker goodness of fit are observed for a small number of fourier components at high ultrasonic pressures and low charge oscillation amplitudes (minimum of $\overline{R}^2_{\mathrm{FS}=2} = 0.61$) (Fig. 2). Consequently, for a given number of fourier components, best performance of the SECONIC-model is expected at lower ultrasonic pressure levels. Next, the dependency of effective parameters on charge oscillation fourier components can be pretabulated (Fig. 3). We observe an inverse proportionality between the effective potential magnitude and the magnitude of the charge oscillation. In contrast, rate functions and membrane voltage oscillations increase with charge oscillations. Consequently, fast charge redistribution will impact neuronal excitability through its influence on the rate functions and the effective potential.

At the lower ultrasonic pressure levels ($P_{\mathrm{US}} \lessapprox 100$ kPa) accurate integration of the PSK-model is obtained within reasonable simulation time (one to two orders of magnitude faster than NICE-MC) (Figs. 6-7). Furthermore, contrary to the NICE-implementation, simulation efficiency depends only on the neuronal activity in both the SECONIC and SONIC models. E.g., at $P_{\mathrm{US}} = 100$ kPa and for $N_{\mathrm{FS}} = 2$, the neuronal response (quantified by the membrane voltage and charge, capacitance, protein state traces, and fourier component trends) is similar to the solution obtained in the NICE-model (Fig. 4). A minor inacurracy, observed at this pressure level, consists of a larger oscillation amplitude of the membrane capacitance, caused by the membrane potential reaching more depolarized values. Discrepancies within the SECONIC solver at higher pressure levels can be explained by the small number of considered fourier components $N_{\mathrm{FS}} = 2$ and by interpolation errors during SECONIC table look-up. Indeed, in Fig. 5 it can be observed that the magnitude of the discrepancy between the calculated ($A_{\mathrm{Q},0} \rightarrow \{A_{\mathrm{Q,i}}, B_{\mathrm{Q,i}}\}$) and exact charge oscillation (Fig. 5(e-f)), is similar to the table look-up error (Fig. 5(c-d)).

B. Computational efficiency of SECONIC - pretabulation

Although efficient simulation of multi-compartmental ultrasonic neuromodulation is possible by pretabulation of voltage fourier components and rate functions, it should be noted that an initial cost is required for the calculation of the look-up tables. Similarly as in the SONIC model for point neurons [39], these tabulation calculations have to be performed only once. More importantly, parallelization of the tabulation is straightforward, as opposed to simulations within the NICE-framework. For the realisation of a morphologically realistic UNMOD model, this parallelization step is indispensible. Indeed, as observed in Figs. 6–7, the simulation time increases with the number of compartments and is already in the order of 5 to 22 hours for the fully sequential two-compartment NICE-model: rough extrapolation predicts excessive simulation times for multi-compartmental morphologically-realistic models with hundreds to thousands of compartments. Another consideration is that the model stiffness is expected to increase with the number of compartments as well, resulting in solver instability or low accuracy (the achievable solver tolerance level is limited by the machine precision in case of very high stiffness) in a model that is not multi-scale optimized. Nevertheless, an important limitation is that, due to the non-linearity of the mechanical Rayleigh-Plesset equation, the independent parameter space scales exponentially with the number of considered fourier series components and acoustic field properties. For example, tabulation with two fourier series components $N_{\mathrm{FS}} = 2$, with 5 and 9 uniformly distributed unique values for the charge oscillation amplitude (0 $\mathrm{nC/cm^2}$ to 100 $\mathrm{nC/cm^2}$ with step 25 $\mathrm{nC/cm^2}$) and phase (0 to 2π with step $2\pi/9$), respectively, and with 30 values for the DC component of the membrane charge (i.e., $5^2 \cdot 9^2 \cdot 30 = 60\ 750$ simulation cases) takes about 3 to 22 hours on one supercluster node (36 processors per node, 2.3 GHz clock rate) for low and high ultrasonic pressure, respectively. Increasing the number of fourier components to $N_{FS} = 3$, higher sampling resolution (e.g., 4 and 2 times more samples for the oscillation amplitude and phase, respectively), or tabulation of 50 ultrasonic intensities, would increase the required computational resources with factors 45, 64 and 50, respectively. Fortunately, a reasonable goodness of fit is already obtained with two fourier series components, except for large pressure amplitudes ($\overline{R}^2 \geq 0.61$).

Besides the number of considered fourier components N_{FS}, also the sampling resolution of the SECONIC look-up tables is important. Here, an optimization is introduced in the trade-off between the required resources for pretabulation, the SECONIC runtime for simulating the neuronal response and the simulation accuracy: in a post-processing step after tabulation, SECONIC-tables are upsampled with a modified Akima method [50], [51] (cfr. section II). This upsampling step is relatively fast and allows to reduce the sampling resolution during the pretabulation step, effectively reducing the required cluster resources. Furthermore, this post-processing step results in a better compromise between the simulation runtime and accuracy for a given table resolution, because the faster (lower order) linear interpolation method is used at runtime. Our results indicate that the modified Akima method is favourable here, as compared to spline or cubic interpolation. As future work, we intend to further investigate the optimal sampling of the independent parameter ranges, the ideal upsampling method and rates (e.g., different interpolation methods might be more suitable for the different table dimensions), number of fourier components, etc., in order to minimize the required resources for the preparation of the look-up tables and the simulation duration for a given level of

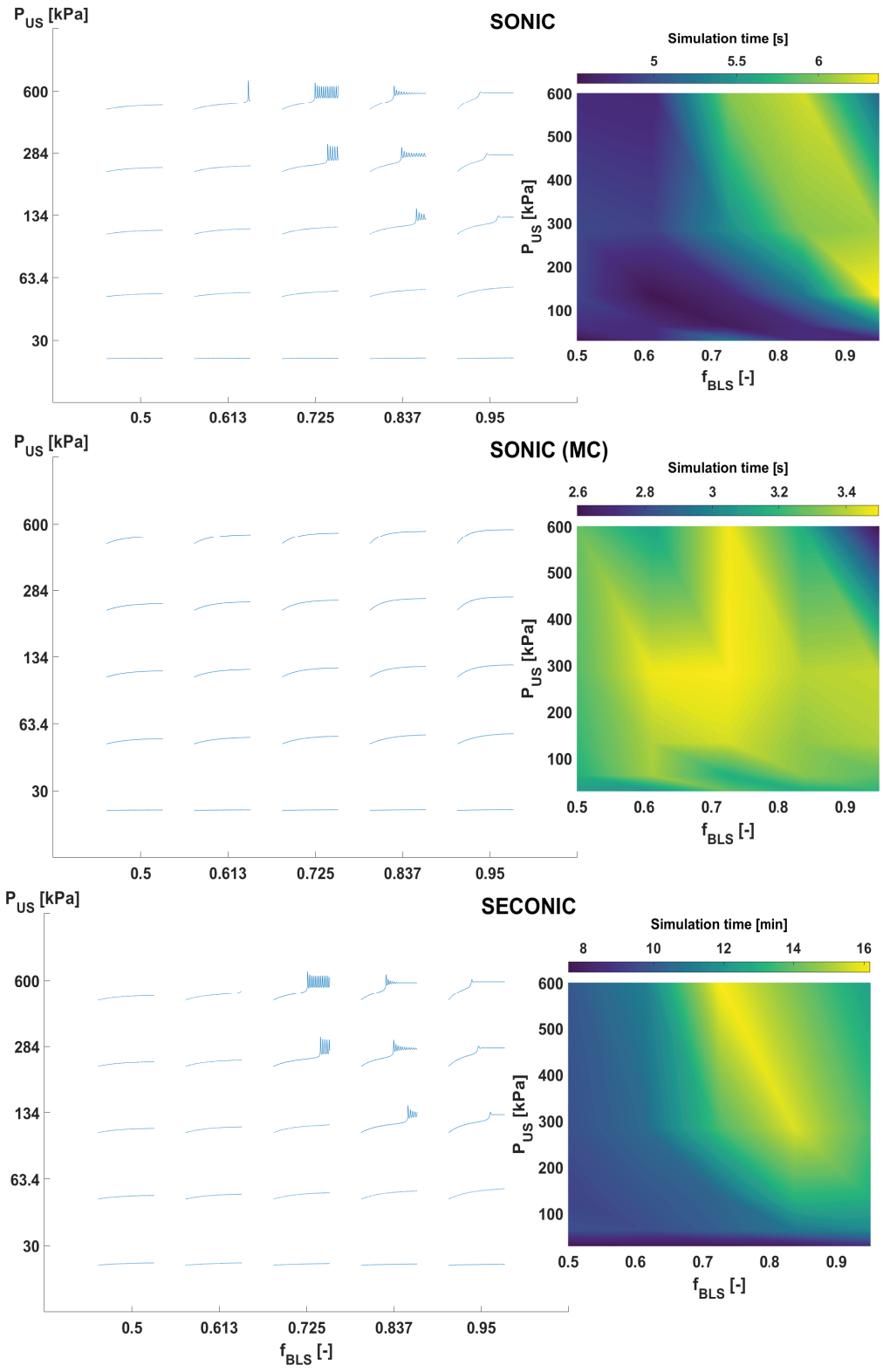

Fig. 8: Accuracy and computational efficiency of the SECONIC-model in the bilayer sonophore-protein structure with partial protein coverage. Response of regular spiking neuron ($f_{\mathrm{US}} = 500$ kHz) for different insonication intensities and sonophore coverage f_{BLS} (left; total membrane charge trace) and corresponding simulation time (right) for the SONIC point-neuron (top), SONIC multi-compartmental (middle), and the SECONIC (bottom; $N_{\mathrm{FS}} = 2$) nanoscale multi-compartmental model. Voltage sensitive membrane conductance gains are restricted to the protein islands in the multi-compartmental models and scaled with the areal protein coverage in point neuron models.

simulation accuracy. This optimization of pretabulation and post-processing settings is likely dependent on the studied ultrasonic waveform and neuron type (e.g., higher number of fourier components at higher ultrasonic pressure levels).

In this context, we also intend to address as future work the limitation that all analysis is performed for continuous-wave UNMOD, because the used regular spiking cortical model is not excitable with pulsed low duty-cycle ultrasound, except at very high intensity [30]. E.g., a comparison with low-threshold spiking cell dynamics, that is sensitive to pulsed ultrasound, will allow us to determine the accuracy and efficiency of SECONIC for pulsed waveforms. Here, one limitation intrinsic to multi-scale optimized frameworks (SONIC or SECONIC) is that transient effects due to discontinuities will not be taken into account (i.e., only the steady-state effect of the discontinuity is expressed in the model). Fortunately, steady state is reached in the majority of cases after one to a few ultrasonic cycles, implying that the multi-scale approximation will only impact the neuronal response at very short duty cycles. Another consideration is that at very short duty cycles, the pulse will have a duration in the same order of magnitude as the SECONIC or SONIC discretization timestep, impacting the solution [39]. However, as the SECONIC-model includes no further approximations on discontinuity-induced transients with respect to the SONIC-model, similar good accuracy of the neuronal response is expected as in [39] for duty cycles above 5% and for a pulse repetition frequency below 10 kHz.

C. Partial protein coverage in the nanoscale BLS

Previous computational studies of the bilayer sonophore with surrounding protein islands, have not yet taken into account the reduction in voltage-sensitive gains with increasing sonophore coverage f_{BLS} [30], [39]. Indeed, the coverage of proteins f_{P} is complementary to that of bilayer sonophores ($f_{\mathrm{P}} = 1 - f_{\mathrm{BLS}}$): this can be taken into account for point neurons by calculating the average conductance ($g_{\mathrm{X}} = f_{\mathrm{P}} g_{\mathrm{X,P}}$, with $g_{\mathrm{X,P}}$ the protein island conductance of ion X, cfr. eq. (3)) and for multi-compartmental neurons by omitting voltage-sensitive gains from the bilayer sonophore compartments. Accounting for partial protein coverage will influence the excitability of the structure as function of the coverage fraction f_{BLS} [46].

In this study, we opted to demonstrate results without taking the consideration of partial protein coverage into account: i.e., voltage-sensitive gains are present over the whole BLS-Protein structure (cfr. Fig. 1(a-b)). Although this assumption is not biologically realistic, this approach allowed us to compare the results more easily with prior work. Here, it is important to note that the main focus of this study is to design a multi-scale optimized framework that accounts for charge oscillations in BLS-models in general. In other words, although we used the bilayer sonophore and surrounding protein islands as a test-model, SECONIC should result in accurate and efficient integration of other multi-compartmental BLS-models as well (e.g., a myelinated axon, in which voltage-sensitive proteins are present at each node of Ranvier compartment). Consequently, the biological realism of the used BLS-Protein model is of lower importance for the interpretation of the performance of SECONIC.

Another consideration is that the BLS-Protein model without accurate description of partial protein coverage demonstrates more clearly the limitation of the SECONIC model at higher ultrasonic pressures ($P_{\mathrm{US}} > 100$ kPa) for $N_{\mathrm{FS}} = 2$, allowing us to discuss the constraints of the SECONIC model with a limited number of fourier components (see also subsection IV-A and IV-B). In contrast, the SECONIC model in the BLS-Protein structure that accounts for partial protein coverage is already very accurate for $N_{\mathrm{FS}} = 2$ over the whole simulated ultrasonic pressure range (up to $P_{\mathrm{US}} = 600$ kPa). For completeness, this result is presented in Fig. 8. In Fig. 8 it can also be observed that the multi-compartmental SONIC model is not excitable when partial protein coverage is taken into account, in agreement with [46].

V. Conclusion

We propose a computationally efficient algorithm SECONIC for multi-compartmental neurons in which fourier series components of the potential and charge are utilized. Each ultrasonic period, the charge oscillation can then be obtained by solving a single algebraic equation.

This extension of the SONIC model to multi-compartmental models is based on the observation that, although charge and voltage oscillate on a timescale set by the ultrasonic frequency, their fourier components are slowly changing. The goodness of the fourier fit is investigated to predict the expected performance of SECONIC: higher ultrasonic pressures will result in greater non-linearity and a larger number of required fourier components. Nevertheless, satisfactory fits are generally already obtained with only two overtones for $P_{\mathrm{US}} \lessapprox 100$ kPa. Subsequently, the dependency of the effective electrodynamical parameters and voltage fourier amplitudes on the charge oscillation amplitude and ultrasonic pressure is studied. Charge oscillations and ultrasonic pressure have opposite effects on the effective capacitance, voltage and displacement: e.g., effective membrane potential is decreased by stronger charge oscillations but increased by larger ultrasonic pressure. Conversely, the potential oscillation amplitudes and effective rate constants experience similar dependency on the ultrasonic intensity and charge oscillation amplitude.

Finally, we demonstrate that the proposed multi-compartmental implementation SECONIC with $N_{\mathrm{FS}} = 2$ yields accurate and fast integration in a nanoscale model of the bilayer sonophore and surrounding proteins for lower ultrasonic pressure. Due to multiscale optimization, simulation efficiency of SECONIC does not depend on the maximal leaflet inflation, but is exclusively determined by the neuronal activity. Higher number of considered fourier components and/or improved resolution of the effective SECONIC-tables is required for accurate simulation at higher ultrasonic pressure levels ($P_{\mathrm{US}} \gtrapprox 100$ kPa). As future work, we intend to apply the SECONIC model for the investigation of ultrasonic neuromodulation by intramembrane cavitation in blue brain project cortical models in the NEURON environment. The subsequent step would then also incorporate FDTD simulations of the induced pressure field in the human brain.

VI. Conflict of interests

The authors declare that there is no conflict of interest regarding the publication of this paper.

References

[1] F. Fry *et al.*, "Production of reversible changes in the central nervous system by ultrasound," *Science*, vol. 127, pp. 83–84, 1958.

[2] E. N. Harvey, "The effect of high frequency sound waves on heart muscle and other irritable tissues," *American Journal of Physiology–Legacy Content*, vol. 91, no. 1, pp. 284–290, 1929.

[3] W. J. Tyler, Y. Tufail, M. Finsterwald, M. L. Tauchmann, E. J. Olson, and C. Majestic, "Remote excitation of neuronal circuits using low-intensity, low-frequency ultrasound," *PloS one*, vol. 3, no. 10, p. e3511, 2008.

[4] Y. Tufail, A. Matyushov, N. Baldwin, M. L. Tauchmann, J. Georges, A. Yoshihiro, S. I. H. Tillery, and W. J. Tyler, "Transcranial pulsed ultrasound stimulates intact brain circuits," *Neuron*, vol. 66, no. 5, pp. 681–694, 2010.

[5] W. Legon, T. F. Sato, A. Opitz, J. Mueller, A. Barbour, A. Williams, and W. J. Tyler, "Transcranial focused ultrasound modulates the activity of primary somatosensory cortex in humans," *Nature neuroscience*, vol. 17, no. 2, p. 322, 2014.

[6] R. L. King, J. R. Brown, W. T. Newsome, and K. B. Pauly, "Effective parameters for ultrasound-induced in vivo neurostimulation," *Ultrasound in medicine & biology*, vol. 39, no. 2, pp. 312–331, 2013.

[7] R. L. King, J. R. Brown, and K. B. Pauly, "Localization of ultrasound-induced in vivo neurostimulation in the mouse model," *Ultrasound in medicine & biology*, vol. 40, no. 7, pp. 1512–1522, 2014.

[8] H. Kim, A. Chiu, S. D. Lee, K. Fischer, and S.-S. Yoo, "Focused ultrasound-mediated non-invasive brain stimulation: examination of sonication parameters," *Brain stimulation*, vol. 7, no. 5, pp. 748–756, 2014.

[9] O. Naor, S. Krupa, and S. Shoham, "Ultrasonic neuromodulation," *Journal of neural engineering*, vol. 13, no. 3, p. 031003, 2016.

[10] H. Baek, K. J. Pahk, and H. Kim, "A review of low-intensity focused ultrasound for neuromodulation," *Biomedical Engineering Letters*, pp. 1–8, 2017.

[11] C. J. Wright, S. R. Haqshenas, J. Rothwell, and N. Saffari, "Unmyelinated peripheral nerves can be stimulated in vitro using pulsed ultrasound," *Ultrasound in medicine & biology*, vol. 43, no. 10, pp. 2269–2283, 2017.

[12] W. Legon, P. Bansal, L. Ai, J. K. Mueller, G. Meekins, and B. Gillick, "Safety of transcranial focused ultrasound for human neuromodulation," *bioRxiv*, p. 314856, 2018.

[13] P. Gaur, K. M. Casey, J. Kubanek, N. Li, M. Mohammadjavadi, Y. Saenz, G. H. Glover, D. M. Bouley, and K. B. Pauly, "Histologic safety of transcranial focused ultrasound neuromodulation and magnetic resonance acoustic radiation force imaging in rhesus macaques and sheep," *Brain Stimulation*, 2020.

[14] W. J. Tyler, "Neuromodulation by focused ultrasound," pp. 1–13, 2019.

[15] J. M. Fine, M. E. Fini, A. S. Mysore, W. J. Tyler, and M. Santello, "Transcranial focused ultrasound enhances behavioral and network mechanisms underlying response inhibition in humans," *bioRxiv*, p. 649665, 2019.

[16] E. Kim, J. Sanchez-Casanova, E. Anguluan, H. Kim, and J. G. Kim, "Mobile wireless low-intensity transcranial ultrasound stimulation system for freely behaving small animals," in *2019 41st Annual International Conference of the IEEE Engineering in Medicine and Biology Society (EMBC)*. IEEE, 2019, pp. 6282–6285.

[17] J. L. Sanguinetti, S. Hameroff, E. E. Smith, T. Sato, C. M. Daft, W. J. Tyler, and J. J. Allen, "Transcranial focused ultrasound to the right prefrontal cortex improves mood and alters functional connectivity in humans," *Frontiers in Human Neuroscience*, vol. 14, p. 52, 2020.

[18] N. Grossman, D. Bono, N. Dedic, S. B. Kodandaramaiah, A. Rudenko, H.-J. Suk, A. M. Cassara, E. Neufeld, N. Kuster, L.-H. Tsai *et al.*, "Noninvasive deep brain stimulation via temporally interfering electric fields," *Cell*, vol. 169, no. 6, pp. 1029–1041, 2017.

[19] T. Tarnaud, W. Joseph, L. Martens, and E. Tanghe, "Computational modeling of ultrasonic subthalamic nucleus stimulation," *IEEE Transactions on Biomedical Engineering*, vol. 66, no. 4, pp. 1155–1164, 2018.

[20] M. A. Samoudi, T. Van Renterghem, and D. Botteldooren, "Computational modeling of a single-element transcranial focused ultrasound transducer for subthalamic nucleus stimulation," *Journal of neural engineering*, 2018.

[21] H. Zhou, L. Niu, L. Meng, Z. Lin, J. Zou, X. Xia, X. Huang, W. Zhou, T. Bian, H. Zheng *et al.*, "Noninvasive ultrasound deep brain stimulation for the treatment of parkinson's disease model mouse," *Research*, vol. 2019, p. 1748489, 2019.

[22] L. Niu, Y. Guo, Z. Lin, Z. Shi, T. Bian, L. Qi, L. Meng, A. A. Grace, H. Zheng, and T.-F. Yuan, "Noninvasive ultrasound deep brain stimulation of nucleus accumbens induces behavioral avoidance," *Science China Life Sciences*, pp. 1–9, 2020.

[23] M. Pernot, J.-F. Aubry, M. Tanter, J.-L. Thomas, and M. Fink, "High power transcranial beam steering for ultrasonic brain therapy," *Physics in medicine and biology*, vol. 48, no. 16, p. 2577, 2003.

[24] G. T. Clement, P. J. White, R. L. King, N. McDannold, and K. Hynynen, "A magnetic resonance imaging–compatible, large-scale array for transskull ultrasound surgery and therapy," *Journal of ultrasound in medicine*, vol. 24, no. 8, pp. 1117–1125, 2005.

[25] L. Marsac, D. Chauvet, B. Larrat, M. Pernot, B. Robert, M. Fink, A.-L. Boch, J.-F. Aubry, and M. Tanter, "Mr-guided adaptive focusing of therapeutic ultrasound beams in the human head," *Medical physics*, vol. 39, no. 2, pp. 1141–1149, 2012.

[26] D. Coluccia, J. Fandino, L. Schwyzer, R. O'Gorman, L. Remonda, J. Anon, E. Martin, and B. Werner, "First noninvasive thermal ablation of a brain tumor with mr-guided focusedultrasound," *Journal of therapeutic ultrasound*, vol. 2, no. 1, p. 17, 2014.

[27] M. L. Prieto, Ö. Oralkan, B. T. Khuri-Yakub, and M. C. Maduke, "Dynamic response of model lipid membranes to ultrasonic radiation force," *PLoS One*, vol. 8, no. 10, p. e77115, 2013.

[28] A. G. Petrov, "Flexoelectricity of model and living membranes," *Biochimica et Biophysica Acta (BBA)-Biomembranes*, vol. 1561, no. 1, pp. 1–25, 2002.

[29] M. Plaksin, S. Shoham, and E. Kimmel, "Intramembrane cavitation as a predictive bio-piezoelectric mechanism for ultrasonic brain stimulation," *Physical review X*, vol. 4, no. 1, p. 011004, 2014.

[30] M. Plaksin, E. Kimmel, and S. Shoham, "Cell-type-selective effects of intramembrane cavitation as a unifying theoretical framework for ultrasonic neuromodulation," *eNeuro*, vol. 3, no. 3, pp. ENEURO–0136, 2016.

[31] B. Krasovitski, V. Frenkel, S. Shoham, and E. Kimmel, "Intramembrane cavitation as a unifying mechanism for ultrasound-induced bioeffects," *Proceedings of the National Academy of Sciences*, vol. 108, no. 8, pp. 3258–3263, 2011.

[32] M. L. Prieto, K. Firouzi, B. T. Khuri-Yakub, and M. Maduke, "Activation of piezo1 but not nav1. 2 channels by ultrasound at 43 mhz," *Ultrasound in medicine & biology*, vol. 44, no. 6, pp. 1217–1232, 2018.

[33] H. Chen, D. Garcia-Gonzalez, and A. Jérusalem, "Computational model of the mechanoelectrophysiological coupling in axons with application to neuromodulation," *Phys. Rev. E*, vol. 99, p. 032406, Mar 2019. [Online]. Available: https://link.aps.org/doi/10.1103/PhysRevE.99.032406

[34] T. Heimburg and A. D. Jackson, "On soliton propagation in biomembranes and nerves," *Proceedings of the National Academy of Sciences of the United States of America*, vol. 102, no. 28, pp. 9790–9795, 2005.

[35] J. Engelbrecht, K. Tamm, and T. Peets, "Modelling of processes in nerve fibres at the interface of physiology and mathematics," *arXiv preprint arXiv:1906.01261*, 2019.

[36] A. Jerusalem, Z. Al-Rekabi, H. Chen, A. Ercole, M. Malboubi, M. Tamayo-Elizalde, L. Verhagen, and S. Contera, "Electrophysiological-mechanical coupling in the neuronal membrane and its role in ultrasound neuromodulation and general anaesthesia," *Acta biomaterialia*, 2019.

[37] A. El Hady and B. B. Machta, "Mechanical surface waves accompany action potential propagation," *Nature communications*, vol. 6, p. 6697, 2015.

[38] T. Tarnaud, W. Joseph, L. Martens, T. Van Renterghem, and E. Tanghe, "Interaction of electrical and ultrasonic neuromodulation: a computational study," *Brain Stimulation: Basic, Translational, and Clinical Research in Neuromodulation*, vol. 12, no. 2, p. 563, 2019.

[39] T. Lemaire, E. Neufeld, N. Kuster, and S. Micera, "Understanding ultrasound neuromodulation using a computationally efficient and interpretable model of intramembrane cavitation," *Journal of Neural Engineering*, 2019.

[40] J. K. Mueller, L. Ai, P. Bansal, and W. Legon, "Numerical evaluation of the skull for human neuromodulation with transcranial focused ultrasound," *Journal of neural engineering*, vol. 14, no. 6, p. 066012, 2017.

[41] T. Tarnaud, W. Joseph, L. Martens, T. Van Renterghem, and E. Tanghe, "Ultrasonic neuromodulation in multi-compartmental neuron models,"

*28th Annual Computational Neuroscience Meeting: CNS*2019*, vol. 20, no. 56, p. 161, 2019.

[42] A. S. Aberra, A. V. Peterchev, and W. M. Grill, "Biophysically realistic neuron models for simulation of cortical stimulation," *Journal of neural engineering*, vol. 15, no. 6, p. 066023, 2018.

[43] H. Markram, E. Muller, S. Ramaswamy, M. W. Reimann, M. Abdellah, C. A. Sanchez, A. Ailamaki, L. Alonso-Nanclares, N. Antille, S. Arsever *et al.*, "Reconstruction and simulation of neocortical microcircuitry," *Cell*, vol. 163, no. 2, pp. 456–492, 2015.

[44] N. T. Carnevale and M. L. Hines, *The NEURON book*. Cambridge University Press, 2006.

[45] M. L. Hines and N. T. Carnevale, "Neuron: a tool for neuroscientists," *The neuroscientist*, vol. 7, no. 2, pp. 123–135, 2001.

[46] T. Tarnaud, W. Joseph, R. Schoeters, L. Martens, and E. Tanghe, "Membrane charge oscillations during ultrasonic neuromodulation by intramembrane cavitation," *IEEE Transactions on Biomedical Engineering*, 2020, under review.

[47] M. Pospischil, M. Toledo-Rodriguez, C. Monier, Z. Piwkowska, T. Bal, Y. Frégnac, H. Markram, and A. Destexhe, "Minimal hodgkin–huxley type models for different classes of cortical and thalamic neurons," *Biological cybernetics*, vol. 99, no. 4-5, pp. 427–441, 2008.

[48] L. F. Shampine and M. W. Reichelt, "The matlab ode suite," *SIAM journal on scientific computing*, vol. 18, no. 1, pp. 1–22, 1997.

[49] R. Ashino, M. Nagase, and R. Vaillancourt, "Behind and beyond the matlab ode suite," *Computers & Mathematics with Applications*, vol. 40, no. 4, pp. 491–512, 2000.

[50] H. Akima, "A new method of interpolation and smooth curve fitting based on local procedures," *Journal of the ACM (JACM)*, vol. 17, no. 4, pp. 589–602, 1970.

[51] ——, "A method of bivariate interpolation and smooth surface fitting based on local procedures," *Communications of the ACM*, vol. 17, no. 1, pp. 18–20, 1974.

[52] J. C. Lagarias, J. A. Reeds, M. H. Wright, and P. E. Wright, "Convergence properties of the nelder–mead simplex method in low dimensions," *SIAM Journal on optimization*, vol. 9, no. 1, pp. 112–147, 1998.